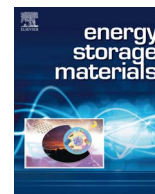




Contents lists available at ScienceDirect

Energy Storage Materials

journal homepage: www.elsevier.com/locate/ensm

A general prelithiation approach for group IV elements and corresponding oxides

Jie Zhao^{a,1}, Jie Sun^{a,1}, Allen Pei^a, Guangmin Zhou^a, Kai Yan^a, Yayuan Liu^a, Dingchang Lin^a, Yi Cui^{a,b,*}

^a Department of Materials Science and Engineering, Stanford University, Stanford, CA 94305, USA

^b Stanford Institute for Materials and Energy Sciences, SLAC National Accelerator Laboratory, 2575 Sand Hill Road, Menlo Park, CA 94025, USA

ARTICLE INFO

Keywords:

Prelithiation
Anode materials
Group IV elements
First cycle Coulombic efficiency

ABSTRACT

Prelithiation of anode materials is an important strategy to compensate for lithium loss as a result of the formation of a solid electrolyte interphase (SEI) at the surface of anodes in lithium-ion batteries. Conventional prelithiation reagents often present serious safety concerns due to the high flammability and unstable chemical nature. Here, we successfully developed a general one-pot metallurgical process to prelithiate group IV elements and their corresponding oxides, yielding prelithiation capacity approaching the theoretical specific capacity. As-synthesized Li_{22}Z_5 alloys and $\text{Li}_{22}\text{Z}_5\text{-Li}_2\text{O}$ composites ($\text{Z} = \text{Si}, \text{Ge}, \text{Sn}$ etc) can serve as prelithiation reagents to increase the first cycle Coulombic efficiency of both graphite and alloy-type anode materials. Among all lithiated group IV alloys, Li_xGe exhibits the best stability under ambient-air conditions, consistent with the simulation results showing the large binding energy between Li and Ge atoms in $\text{Li}_{22}\text{Ge}_5$ crystal. Metallurgical lithiation of ZO_2 results in composites with homogeneously dispersed reactive Li_xZ nanodomains embedded in a robust Li_2O matrix which effectively suppresses the oxidation process. $\text{Li}_{22}\text{Z}_5\text{-Li}_2\text{O}$ composites further improve the ambient-air stability because the strong binding between O atoms in Li_2O and Li atoms in Li_{22}Z_5 stabilizes the reactive Li_{22}Z_5 nanodomains. These results allow us to identify the prelithiation reagents with the optimal stability in air, thereby simplifying the requirement on the industrial electrode fabrication environment.

1. Introduction

The emerging electric vehicles market has stimulated intensive research on low-cost lithium-ion (Li-ion) batteries with high energy density and long cycle life [1–3]. Currently, existing Li-ion batteries are produced in the discharged state with Li pre-stored in the cathode due to the air stability of the lithiated cathode materials [4,5]. During battery operation, organic electrolytes are not stable and decompose to form an SEI layer on the surface of electrodes at the working potential of the anode [6,7]. This irreversible formation of SEI consumes Li from cathode materials and occurs mainly during the first lithiation process, resulting in an appreciable loss of active cathode materials and low 1st cycle Coulombic efficiency (CE) [8,9]. The 1st cycle CE of commercial graphite electrodes is typically around 90% [10,11], whereas 1st cycle CEs for high-capacity alloy anodes including Si, Ge and Sn are usually lower than 80% due to the increased surface area of the nanostructured electrodes utilized to improve cycling performance of alloy anodes [12–14]. These low 1st cycle CEs impose a significant hurdle in constructing full-cells for

practical applications because the Li consumption at the anode side necessitates an excess amount of cathode active material solely to compensate for the first cycle losses, leading to a reduced total energy density [15]. Moreover, cathode capacity loading is limited by coating thickness due to kinetic factors [16].

Prelithiation is a common way to improve the 1st cycle CE of Li-ion batteries. Cathode prelithiation was previously achieved by the addition of Li-rich compounds such as Li_2NiO_2 [17], Li_6CoO_4 [18], metal/ Li_2O composites [19], and metal/LiF composites [20]. However, prelithiation capacities of these materials are generally lower than 1000 mAh/g. Li_2O and Li_3N powders exhibit much higher specific capacities (> 1400 mAh/g), but the use of these additives is accompanied with the evolution of O_2 and N_2 gas, respectively [21–23]. In terms of anode prelithiation, Si nanowires and Sn-C electrode were electrochemically lithiated by directly shorting with Li metal [24,25]. Choi's group further improved this electrochemical lithiation approach in a controlled manner by shorting silicon monoxide with Li metal in the presence of an optimized circuit

* Corresponding author at: Department of Materials Science and Engineering, Stanford University, Stanford, CA 94305, USA.

E-mail address: yicui@stanford.edu (Y. Cui).

¹ These authors contributed equally.

<http://dx.doi.org/10.1016/j.ensm.2017.06.013>

Received 31 January 2016; Received in revised form 22 March 2017; Accepted 22 June 2017

2405-8297/ © 2017 Published by Elsevier B.V.

resistance and simultaneously monitoring the voltage between both electrodes [26]. Microscale stabilized lithium metal powder (SLMP, FMC Lithium Corp) [27–29], and a polymer protected Li metal layer [30] have been also effectively employed to compensate for the first cycle irreversible capacity loss of various anode materials including graphite and Si. Recently, we demonstrated that metallurgically synthesized Li_xSi nanoparticles (NPs) can serve as a high-capacity prelithiation reagent to effectively increase the 1st cycle CE of anode materials [31]. Li_2O and artificial-SEI coatings have been utilized to increase the stability of Li_xSi NPs in air with low humidity level (< 10% relative humidity (RH)) [32]. Furthermore, metallurgically lithiated SiO_x developed a unique composite structure of homogeneously dispersed reactive Li_xSi nanodomains embedded in a robust Li_2O matrix which was found to further improve ambient-air stability (~ 40% RH) [33]. Group IV elements such as Ge and Sn also have relatively high specific capacities (1640 mAh/g for Ge, and 993 mAh/g for Sn) and similar volumetric capacities to Si (2574 mAh/cm³ for Si, 2275 mAh/cm³ for Ge, and 2111 mAh/cm³ for Sn), making them also suitable for pre-storing Li [15,34–36]. As such, the strategy of embedding active lithium alloys in a robust Li_2O matrix is also attractive for other group IV elements and is predicted to stabilize the lithiated group IV alloys.

Herein, we developed a one-pot metallurgical process to synthesize Li_{22}Z_5 alloys (Z = Ge and Sn) and $\text{Li}_{22}\text{Z}_5\text{-Li}_2\text{O}$ composites by using Z and ZO_2 as the source materials, respectively. Both Li_{22}Z_5 alloys and $\text{Li}_{22}\text{Z}_5\text{-Li}_2\text{O}$ composites are reactive enough to prelithiate various anode materials such as graphite and Sn, thereby achieving high 1st cycle CEs of > 100%. Among all lithiated group IV alloys, Li_xGe NPs exhibits the best stability under ambient-air conditions, consistent with the simulation results showing that Ge atoms in the cubic $\text{Li}_{22}\text{Ge}_5$ crystal have the strongest bonding with Li atoms. $\text{Li}_{22}\text{Z}_5\text{-Li}_2\text{O}$ composites further enhanced the air stability over their corresponding Li_{22}Z_5 alloys thanks to the strong binding between O atoms in Li_2O and Li atoms in Li_{22}Z_5 .

2. Materials and methods

2.1. Synthesis of Li_xZ alloys and $\text{Li}_x\text{Z-Li}_2\text{O}$ composites

Ge and GeO_2 microparticles (Sigma Aldrich) were first ground to obtain fine powders by planetary ball milling operated at a grinding speed of 400 rpm for 24 h. SnO_2 nanoclusters were prepared via a bio-inspired hydrothermal method in the presence of tris(hydroxymethyl) aminomethane (THAM, Sigma Aldrich) [37]. 0.27 g of $\text{Na}_2\text{SnO}_3 \cdot 3\text{H}_2\text{O}$ (Sigma Aldrich) and 0.2 g of THAM were first dissolved into 35 ml of distilled H_2O , and then transferred into a 40 mL Teflon-lined stainless-steel autoclave. The autoclave was kept at 120 °C for 10 h. Finally, the obtained white sample was washed with deionized water and pure ethanol. The starting materials including Ge NPs, GeO_2 NPs, Sn NPs (Sigma Aldrich) and SnO_2 nanoclusters were dried under vacuum for 48 h and then heated to 120 °C in the argon glove box (O_2 level < 1.2 ppm, and H_2O level < 0.1 ppm) for 12 h to remove trapped water and oxygen. A mixture of ball-milled Ge NPs and Li metal (99.9%, Alfa Aesar) (1177:500 mg, which is determined by the chemical reaction in Supplementary information, Fig. S1) was heated at 250 °C under mechanical stirring inside a tantalum crucible at 200 rpm for 2 days and then quenched to obtain the crystalline phase of $\text{Li}_{22}\text{Ge}_5$ in the argon glovebox. Under similar conditions, GeO_2 NPs or SnO_2 nanoclusters were reacted with molten Li to form $\text{Li}_x\text{Ge-10Li}_2\text{O}$ or $\text{Li}_x\text{Sn-10Li}_2\text{O}$ composite, respectively. The weight ratio of starting materials to Li metal is also determined by the chemical equation in Supplementary information, Fig. S1. The synthesis condition of Li_xSn alloy is slightly different because of the low melting point of Sn compared with other starting materials. The alloying temperature should be maintained between the melting points of Li metal and Sn (180°C and 232°C, respectively) to ensure the preservation of the morphology of Sn NPs.

2.2. Electrochemical characterization

Sn NPs, graphite, carbon black (Super P, TIMCAL, Switzerland), and polyvinylidene fluoride binder (PVDF, Kynar HSV 900) were dried under vacuum for 24 h to remove trapped water. To prepare the working electrodes, various materials were dispersed uniformly in tetrahydrofuran (THF, Sigma Aldrich) to form a slurry (Anode materials and mass ratio are based on specific cells.). The slurry was then cast onto a thin copper foil and dried under vacuum. Coin-type 2032 cells were assembled in an argon glovebox using Li metal as counter/reference electrode. The electrolyte is 1.0 M lithium hexafluorophosphate (LiPF_6) in 1:1 v/v ethylene carbonate/diethyl carbonate (BASF, LP 40). Cyclic voltammetry measurements were carried out on a BioLogic VMP3 system. Galvanostatic cycling was carried out using an MTI 8 Channel battery tester and a 96-channel battery tester (Arbin Instruments). The total mass loading of Li_xZ NPs or $\text{Li}_x\text{Z-Li}_2\text{O}$ composites based anode was 2.0~3.0 mg/cm² and the typical mass loading of the graphite based anode was ~ 5 mg/cm².

3. Results and discussion

3.1. Density functional theory simulation

To study the stability of different Li_xZ alloys (Z = Si, Ge and Sn) in ambient-air conditions, we performed density functional theory (DFT) simulations to calculate the interaction between Z atoms and Li atoms in the cubic Li_{22}Z_5 crystal. The binding energy (E_b) of Li with Si, Ge, and Sn was obtained using CASTEP simulation package in the framework of DFT. Although Li alloyed with group IV elements to form the Li-richest alloys with the same formula, the crystal structures are slightly different. For simplicity, we selected the similar simulation fragments of $\text{Li}_8\text{Si}_{10}$ pseudo-tetrahedron from cubic $\text{Li}_{22}\text{Si}_5$, $\text{Li}_5\text{Ge}_{10}$ pseudo-tetrahedron from cubic $\text{Li}_{22}\text{Ge}_5$, and Li_4Sn_6 octahedron from cubic $\text{Li}_{22}\text{Sn}_5$ ($\text{Li}_{17}\text{Sn}_4$) as shown in Fig. 1a. Li was calculated to have a binding energy of -2.98 eV with Ge, which is higher than that of the other two species (Si: -0.80 eV, Sn: -2.15 eV). According to this definition, a more negative value of E_b indicates a stronger binding or a more energetically favorable reaction. Based on the DFT simulation results, $\text{Li}_{22}\text{Ge}_5$ is the most thermally stable alloy in the crystalline Li_{22}Z_5 family. Previously, we performed DFT simulations to calculate the interaction energy between O atoms in Li_2O and Li atoms in $\text{Li}_{22}\text{Si}_5$ [33]. The binding energies between O atoms of Li_2O and surface Li atoms of $\text{Li}_{22}\text{Si}_5$ are much larger than the binding energy between Li and Si atoms in $\text{Li}_{22}\text{Si}_5$ crystal. In $\text{Li}_x\text{Si-Li}_2\text{O}$ composites, Li_xSi nanodomains are uniformly embedded in a robust Li_2O matrix, providing more binding between O in Li_2O and Li in $\text{Li}_{22}\text{Si}_5$ which effectively stabilizes the Li in $\text{Li}_{22}\text{Si}_5$ nanodomains. It is anticipated that this effect is also applicable to other $\text{Li}_x\text{Z-Li}_2\text{O}$ composites improving their stability beyond that of pure Li_xZ alloys.

3.2. Synthesis and characterizations of Li_xZ alloys and $\text{Li}_x\text{Z-Li}_2\text{O}$ composites

To confirm the DFT results, Li_xZ alloys and $\text{Li}_x\text{Z-Li}_2\text{O}$ composites were synthesized. Ge NPs and GeO_2 NPs were used as the starting materials to form the Li_xGe alloy and $\text{Li}_x\text{Ge-Li}_2\text{O}$ composite, respectively. A mixture of ball-milled Ge NPs and Li metal (1177:500 mg) was heated at 250 °C under mechanical stirring inside a tantalum crucible at 200 rpm for 2 days and then quenched to obtain the crystalline phase of $\text{Li}_{22}\text{Ge}_5$ in an argon glovebox (Fig. 1b). Under the same conditions, ball-milled GeO_2 NPs were reacted with molten Li to form the $\text{Li}_x\text{Ge-Li}_2\text{O}$ composite. Scanning electron microscopy (SEM) was utilized to characterize the morphology of the Ge and GeO_2 NPs before and after lithiation. After ball milling, the size of Ge NPs is in the range of 40–220 nm, while that of GeO_2 NPs is in the range of 110–370 nm as shown in Fig. 2a and d. The sizes of the derived Li_xGe alloy and

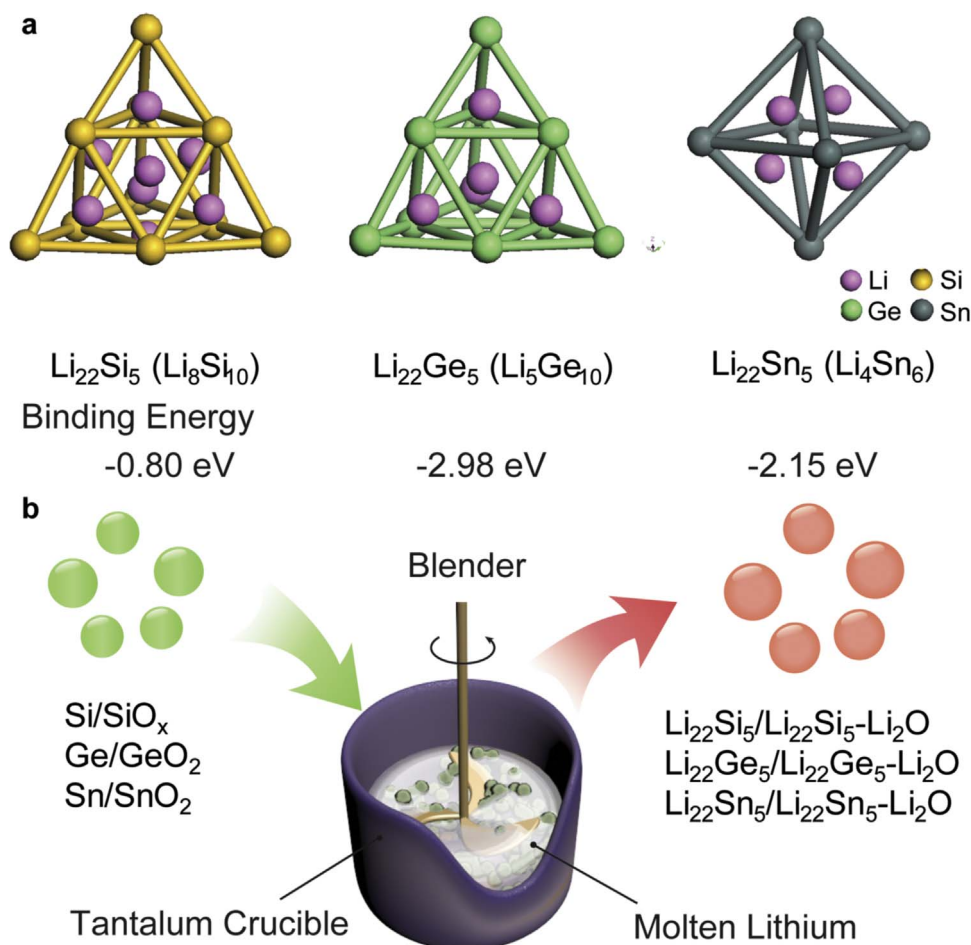


Fig. 1. (a) The $\text{Li}_8\text{Si}_{10}$ pseudo-tetrahedron from cubic $\text{Li}_{22}\text{Si}_5$, $\text{Li}_5\text{Ge}_{10}$ pseudo-tetrahedron from cubic $\text{Li}_{22}\text{Ge}_5$, and Li_4Sn_6 octahedron from cubic $\text{Li}_{22}\text{Sn}_5$ were selected as the simulation units to calculate the binding energy (E_b) of Li with Z (Z = Si, Ge and Sn). (b) Schematic diagram showing a one-pot metallurgical process to synthesize Li_{22}Z_5 alloys and $\text{Li}_{22}\text{Z}_5\text{-Li}_2\text{O}$ composites by using Z and ZO_2 as the starting materials, respectively.

$\text{Li}_x\text{Ge-Li}_2\text{O}$ composite were larger than those of the starting materials because of the volume expansion and some degree of particle aggregation during the metallurgical process (Fig. 2b and e). The size distributions of Ge and GeO_2 NPs before and after thermal lithiation are shown in Supplementary information, Fig. S2. X-ray diffraction (XRD) confirms the crystalline nature of ball-milled Ge powder (PDF no. 00-004-0545) and a small portion of GeO_2 (PDF no. 00-036-1463) resulting from the high-energy ball-milling process in air (Fig. 2c, upper). XRD confirms the complete transformation of Ge in both Ge powder and the intrinsic oxide GeO_2 to crystalline $\text{Li}_{22}\text{Ge}_5$ (PDF no. 01-081-6059) during the thermal alloying process (Fig. 2c, bottom). The small peaks of Li_2O (PDF no. 00-012-0254) come from the conversion of the small amount of intrinsic oxide GeO_2 . XRD (Supplementary information, Fig. S3) also shows the complete formation of crystalline $\text{Li}_{22}\text{Ge}_5$ and Li_2O during the thermal alloying process of GeO_2 powder and molten Li. The only difference is the much higher percentage of Li_2O in the final product. Kapton tapes covered the XRD samples to suppress side reactions in the air, contributing the broad background of XRD patterns.

$\text{Li}_{22}\text{Sn}_5$ alloy was obtained at similar synthesis conditions as $\text{Li}_{22}\text{Ge}_5$ alloy by using Sn NPs as the starting material. The only difference is the alloying temperature should be maintained between the melting points of Li metal and Sn to ensure the preservation of the morphology of Sn NPs. Both SEM (Fig. 2f) and TEM (Supplementary information, Fig. S4a) images confirm that the Sn NPs have sizes less than 200 nm. After metallurgical lithiation, the shape of the NPs is retained, whereas the particle sizes are larger due to volume expansion and some aggregation (Fig. 2g and Supplementary information, Fig. S4b). XRD confirms the

transformation from Sn (PDF no. 00-004-0673) to $\text{Li}_{22}\text{Sn}_5$ (PDF no. 01-081-6569) after thermal alloying with molten Li (Fig. 2h). The small amount of Li_2O again arises from the intrinsic monoxide SnO (PDF no. 04-005-4541) in Sn NPs. The hydrothermal-synthesized SnO_2 nanoclusters are uniform both in size (~ 50 nm) and shape as confirmed by SEM and TEM (Fig. 2i and Supplementary information, Fig. S5a). The magnified TEM image (Supplementary information, Fig. S5b) shows that the clusters are composed of ultrafine crystallites with size of 10 nm. The lattices with plane spacing of 3.34 nm and 2.64 nm are observed, corresponding to the SnO_2 (110) and (101) lattice planes, respectively. The monodisperse SnO_2 nanoclusters were utilized as the precursor for the $\text{Li}_x\text{Sn-Li}_2\text{O}$ composite. After thermal lithiation, the morphology of SnO_2 nanoclusters was preserved, whereas the size of the clusters slightly increased to 75 nm because of volume expansion (Fig. 2j). XRD of lithiated SnO_2 shows the same final products as lithiated Sn NPs with a higher percentage of the Li_2O phase (Supplementary information, Fig. S6).

3.3. Electrochemical characterizations of Li_xZ alloys and $\text{Li}_x\text{Z-Li}_2\text{O}$ composites

To study the electrochemical properties of the Li_xZ alloys and $\text{Li}_x\text{Z-Li}_2\text{O}$ composites, half cells were fabricated with Li metal as a counter electrode. Li_xZ alloys or $\text{Li}_x\text{Z-Li}_2\text{O}$ composites were mixed with Super P and PVDF (65:20:15 by weight) in THF to form a slurry, which was then drop cast on a thin copper foil and dried under vacuum. Because of the high reactivity of Li_xZ alloys and $\text{Li}_x\text{Z-Li}_2\text{O}$ composites, solvents with higher polarity were avoided. To measure the prelithiation

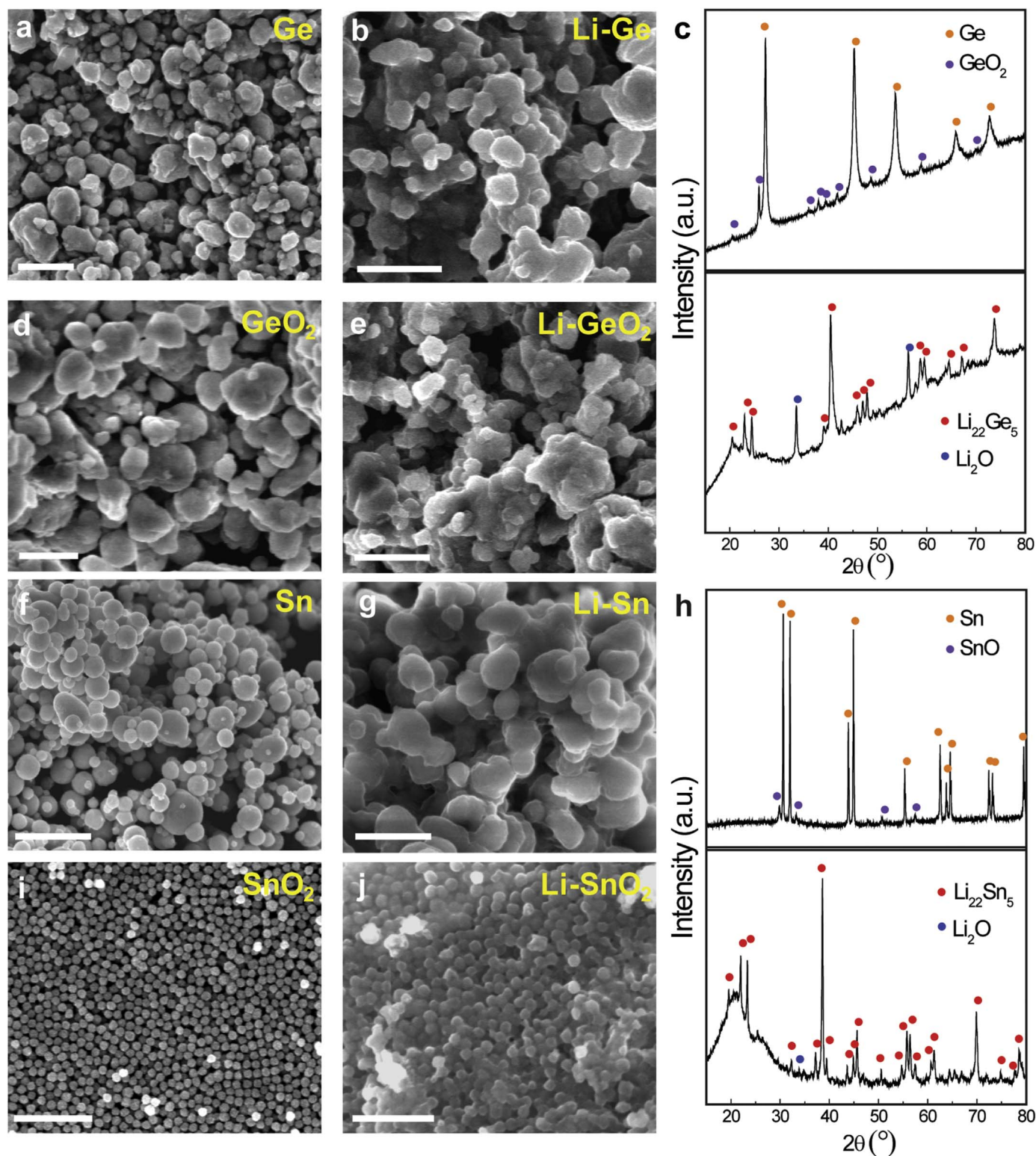


Fig. 2. (a, b) SEM images of Ge NPs (a) before and (b) after thermal lithiation. (c) XRD patterns of Ge NPs before (upper) and after lithiation (bottom). (d, e) SEM images of GeO₂ NPs (d) before and (e) after thermal lithiation. (f, g) SEM images of Sn NPs (f) before and (g) after thermal lithiation. (h) XRD patterns of Sn NPs before (upper) and after lithiation (bottom). (i, j) SEM images of SnO₂ nanoclusters (i) before and (j) after thermal lithiation. Scale bar, 500 nm.

capacities of the Li_xGe alloy and Li_xGe-Li₂O composite, the electrodes were charged to 1.5 V directly at a slow rate of C/20 (1 C = 1640 mA/g for Ge and 1126 mA/g for GeO₂). The prelithiation capacities were 1335 mAh/g and 892 mAh/g based on the masses of Ge and GeO₂ in the electrode, respectively (Fig. 3a). Similarly, charged to 2 V at a rate of C/20, the Li_xSn alloy and Li_xSn-Li₂O composite electrodes had

extraction capacities of 910 mAh/g and 695 mAh/g, approaching the theoretical specific capacities of Sn and SnO₂, respectively (The specific capacity is estimated on the basis of the mass of Sn or SnO₂ in the electrode. 1 C = 990 mA/g for Sn and 782 mA/g for SnO₂, Fig. 3b). The voltage profile of the lithiated SnO₂ electrode exhibits the same plateaus as that of the lithiated Sn electrode, reflecting the same active

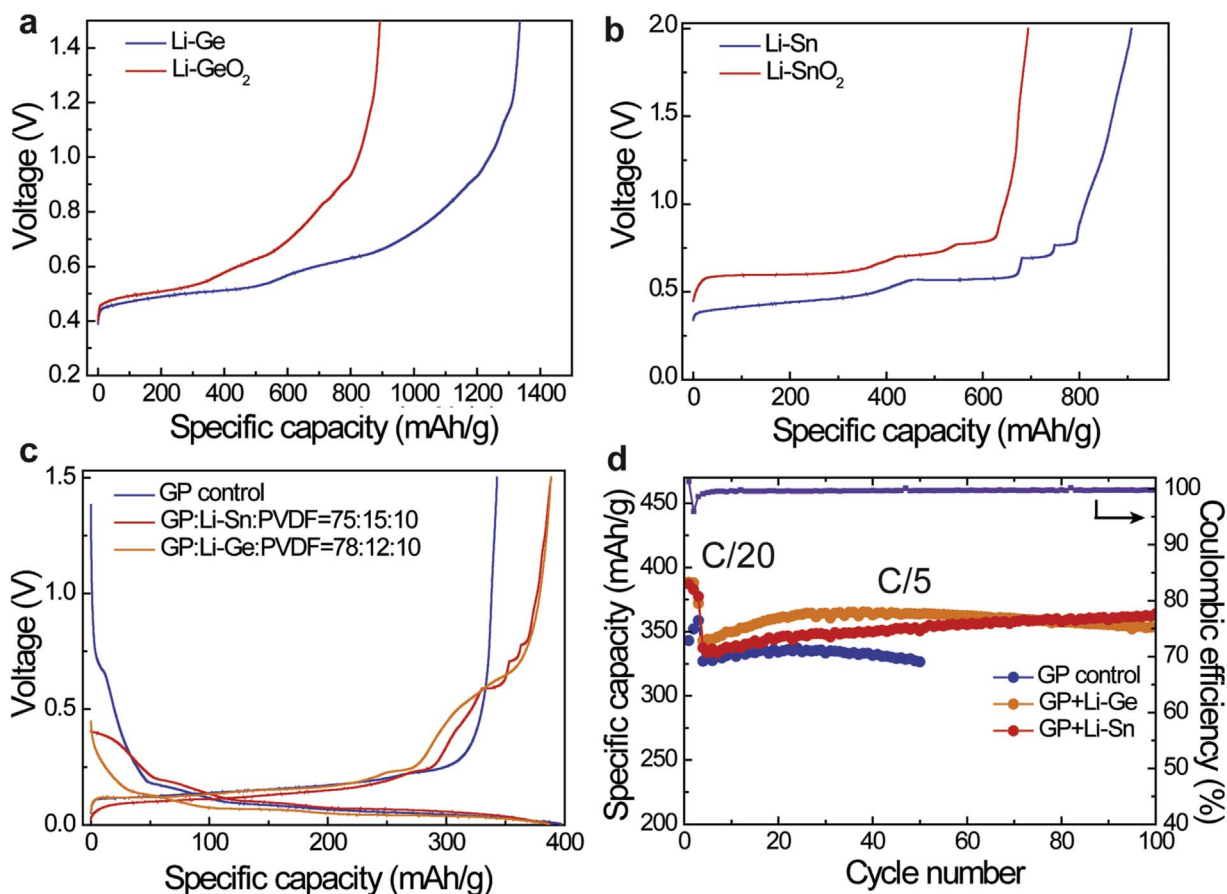


Fig. 3. (a) First-cycle delithiation capacities of lithiated Ge NPs (blue) and lithiated GeO_2 NPs (red). The capacity is based on the mass of Ge or GeO_2 in the anode. (b) First-cycle delithiation capacities of lithiated Sn NPs (blue) and lithiated SnO_2 NPs (red). The capacity is based on the mass of Sn or SnO_2 in the anode. (c) First-cycle voltage profiles of graphite/lithiated Sn cell (75:15 by weight, red), graphite/lithiated Ge cell (78:12 by weight, orange) and graphite control cell (blue). The capacity is based on the total mass of the active materials, including graphite, Ge, and Sn in Li_xZ alloys (Z = Ge and Sn). (d) Cycling performance of graphite/lithiated Sn cell (red), graphite/lithiated Ge cell (orange) and graphite control cell (blue) at C/20 for the first three cycles and C/5 for the following cycles (1 C = 370 mA/g of graphite). The purple line is the Coulombic efficiency of the graphite/lithiated Sn cell. The total mass loading of Li_xZ NPs or $\text{Li}_x\text{Z-Li}_2\text{O}$ composites based anode was 2.0–3.0 mg/cm^2 and the mass loading of the graphite based anode was $\sim 5 \text{ mg}/\text{cm}^2$. (For interpretation of the references to color in this figure legend, the reader is referred to the web version of this article)

material compositions of the electrodes. Consistently, the cyclic voltammetry (CV) profile of the lithiated SnO_2 electrode shows the typical shape of a Sn electrode (Supplementary information, Fig. S7) [38].

Because of their low potential and high capacity, Li_xZ alloys and $\text{Li}_x\text{Z-Li}_2\text{O}$ composites are reactive enough to be used as prelithiation reagents to increase the 1st cycle CE of different anode materials, such as graphite and Sn. In Fig. 3c, the blue voltage profile of a graphite control cell reveals a plateau between 0.2 and 0.7 V, corresponding to SEI formation during the first lithiation process. As a result, the 1st cycle CE of the graphite control cell is only 87.4% as measured in the voltage window of 0.005–1.5 V. To confirm the prelithiation effect, Li_xZ alloy was mixed with graphite flakes and PVDF at a certain ratio in a slurry to form the working electrodes. On the addition of organic electrolytes, Li_xZ alloy was spontaneously activated, providing additional Li ions to the anode for SEI formation and partial lithiation of the active anode materials. After cell assembly, it takes about 6 h for the potential of electrodes to reach a steady state. With the addition of Li_xSn NPs, the open-circuit voltage (OCV) of graphite/ Li_xSn cell (graphite flakes: Li_xSn :PVDF = 75:15:10 by weight) is decreased to 0.4 V, significantly lower than the 1.4 V of the control cell, indicating partial prelithiation of the graphite flakes. The capacity of Li_xSn NPs compensates the irreversible capacity loss of the graphite in the first cycle, increasing the 1st cycle CE to 100.3%. With the relatively higher specific capacity, a smaller amount (12 wt%) of Li_xGe NPs is needed for prelithiation of graphite flakes to reach a similar 1st cycle CE of 100.6%. With the addition of Li_xZ NPs,

graphite/ Li_xZ cells exhibit consistent higher capacity and stable cycling at C/20 for the first three cycles and C/5 for the following cycles (1 C = 372 mA/g of graphite). The capacity is based on the total mass of graphite flakes and Z in Li_xZ NPs. Fig. 3d). Both as-synthesized Li_xGe and Li_xSn alloys are in nanoparticle form and tend to be embedded in the interparticle spaces between microscale graphite flakes. Since Li_xGe and Li_xSn NPs are already in their fully expanded states, they will not squeeze graphite flakes during lithiation and delithiation, contributing to the stable cycling of graphite/ Li_xZ cells. Aside from intercalation-type graphite anodes, prelithiation using Li_xZ NPs is also applicable to high-capacity alloy-type anodes such as Sn. Prelithiation of Sn NPs with Li_xSn NPs (mass ratio 60:20) shows consistent results, increasing 1st cycle CE from 77.7% to 94.1% (Supplementary information, Fig. S8).

3.4. Air-stability of Li_xZ alloys and $\text{Li}_x\text{Z-Li}_2\text{O}$ composites

The stability of Li_xZ alloys and $\text{Li}_x\text{Z-Li}_2\text{O}$ composites was tested under different air conditions to confirm the DFT simulation results. To compare their dry-air stability, different Li_xZ alloys were stored in a dry room (dew point = $-50 \text{ }^\circ\text{C}$) for 5 days. The remaining capacity of Li_xSn NPs exposed to dry air over many days were studied by charging the Li_xSn NPs electrodes to 2 V at a low rate of C/20 (Fig. 4a). After 5 days' exposure, Li_xSn NPs exhibit a high capacity of 845 mA/h/g, corresponding to a capacity retention of 93%. Among the Li_xZ alloys, Li_xGe shows the best dry-air stability with negligible (6.5%) capacity decay after 5 days of exposure, consistent with the simulation results indicating that

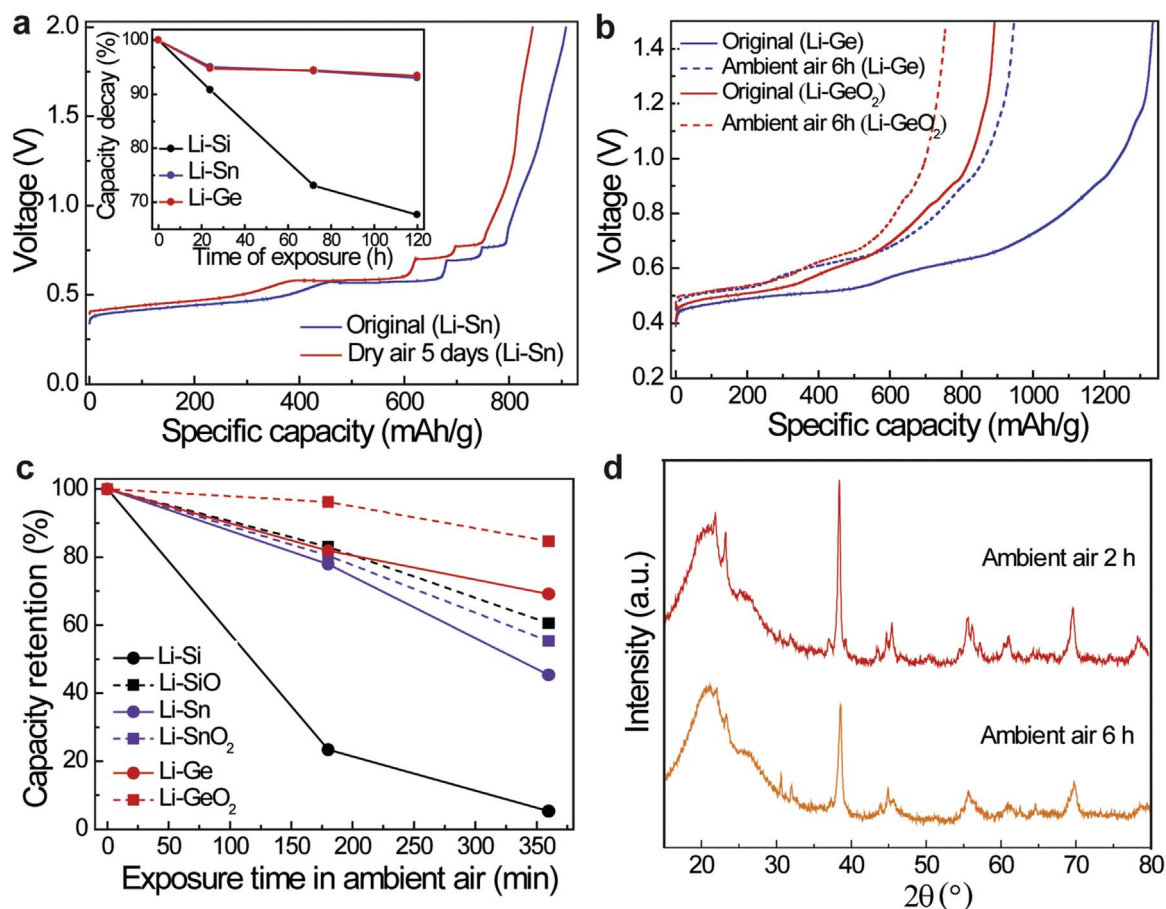


Fig. 4. (a) First-cycle delithiation capacities of lithiated Sn NPs before (blue) and after (red) exposure to dry-air condition for 5 days. The inset shows the trend of capacity decay of lithiated Si (black), Sn (purple) and Ge (red) NPs. (b) First-cycle delithiation capacities of lithiated Ge NPs (blue) and lithiated GeO₂ NPs (red) before (solid) and after (dash) exposure to ambient-air condition (~40% RH) for 6 h. (c) Capacity retention of lithiated Si (black, solid), SiO (black, dash), Sn (purple, solid), SnO₂ (purple, dash), Ge (red, solid) and GeO₂ (red, dash) NPs exposed to ambient-air condition with varying duration. (d) XRD patterns of lithiated Sn NPs exposed to ambient-air condition for 2 h (upper) and 6 h (bottom). (For interpretation of the references to color in this figure legend, the reader is referred to the web version of this article)

Ge atoms in the Li₂₂Ge₅ crystal has the strongest bonding with Li atoms which stabilizes active Li. The trend of capacity decay of Li_xGe and Li_xSn is much slower than that of Li_xSi NPs, which loses 33% capacity after 5 days (inset of Fig. 4a). To further challenge the stability of Li_xGe, Li_xGe NPs was exposed to ambient air (~40% RH) for 6 h, exhibiting a high extraction capacity of 947 mAh/g (30% capacity loss, Fig. 4b). Although the specific capacity is relatively lower, Li_xGe-Li₂O NPs exhibit superior ambient-air stability with a higher capacity retention of 85% (15% capacity loss) compared to bare Li_xGe NPs. The capacity retentions of lithiated Z NPs and their corresponding oxides in ambient air after various durations were studied as shown in Fig. 4c. Similar to the trends in dry air conditions, the capacity decay of Li_xGe and Li_xSn NPs is much slower than that of Li_xSi NPs, because of the stronger binding between Li atoms and Ge or Sn atoms in the corresponding cubic crystals. No new peaks are present in the XRD pattern of Li_xSn NPs exposed to ambient air for 2 h (Fig. 4d). The XRD pattern reveals small peaks belonging to Li(OH)·H₂O (PDF no. 04-010-4336), and the intensity of Li₂₂Sn₅ peaks drops significantly after being exposed to ambient air for 6 h. Consistently, Li_xSn NPs show a high extraction capacity of 707 mAh/g after 2 h of exposure and only 45% capacity retention after 6 h (Supplementary information, Fig. S9). It is necessary to notice that Li_xZ-Li₂O composites consistently exhibit superior ambient-air stability as compared with bare Li_xZ NPs. Similar to the Li_xSi-Li₂O composite, thermal lithiation of ZO₂ results in a composite with homogeneously dispersed reactive Li_xZ nanodomains embedded in a robust Li₂O matrix, providing more binding between O atoms in Li₂O and Li atoms in Li₂₂Z₅, which effectively stabilizes the Li

in Li_xZ nanodomains. Usually, Li₂₂Z₅ alloys have a thin coating of Li₂O, that serves as a passivation shell slowing down the corrosion reaction in the air [31]. However, the highly robust and crystalline Li₂O matrix formed at high temperature is dense enough to prevent side reactions in the air compared with Li₂O coating formed at room temperature. For core-shell structure, any pinhole will provide a pathway for inner Li_xZ to react with the air and thus, reduce the capacity. In the Li₂₂Z₅-Li₂O composites, Li₂₂Z₅ nanodomains are uniformly embedded in a robust Li₂O matrix, such that each Li₂₂Z₅ nanodomain has localized Li₂O protection. Even if some Li_xZ domains are inactivated by the presence of pinholes on the surface, the inner Li₂O still serves as a localized anti-corrosion layer to prevent inner Li_xZ domains from additional corrosion.

4. Conclusions

In conclusion, we have developed a general prelithiation approach to obtain Li₂₂Z₅ alloys (Z = Ge and Sn) and Li₂₂Z₅-Li₂O composites using Z and ZO₂ as starting materials, respectively. This approach is general applicable to Z and oxides with complex nanostructures. Because of their high capacity and low chemical potential, both Li₂₂Z₅ alloys and Li₂₂Z₅-Li₂O composites are reactive enough to prelithiate graphite and alloy-type anode materials. Among all lithiated group IV alloys, Li_xGe alloy exhibits the best ambient-air stability, consistent with the simulation results showing the large binding energy between Li and Ge atoms in Li₂₂Ge₅ crystal. Li₂₂Z₅-Li₂O composites consistently exhibit better ambient-air stability than their correspond-

ing Li_{22}Z_5 alloys due to the strong binding between O atoms in the Li_2O and Li atoms in Li_{22}Z_5 which stabilizes the reactive Li_{22}Z_5 nanodomains. These guiding principles point out the prelithiation reagents with the best air stability, simplifying requirements for industrial battery fabrication environments, which in turn, can decrease battery manufacturing costs.

Acknowledgements

We acknowledge the support from the Assistant Secretary for Energy Efficiency and Renewable Energy, Office of Vehicle Technologies, Battery Materials Research Program of the U.S. Department of Energy.

Appendix A. Supporting information

Supplementary data associated with this article can be found in the online version at doi:10.1016/j.ensm.2017.06.013.

References

- [1] B. Dunn, H. Kamath, J.M. Tarascon, Electrical energy storage for the grid: a battery of choices, *Science* 334 (2011) 928–935.
- [2] J.B. Goodenough, Evolution of strategies for modern rechargeable batteries, *Acc. Chem. Res.* 46 (2013) 1053–1061.
- [3] Y. Sun, N. Liu, Y. Cui, Promises and challenges of nanomaterials for lithium-based rechargeable batteries, *Nat. Energy* 1 (2016) 16071.
- [4] G. Crabtree, E. Kocs, L. Trahey, The energy-storage frontier: lithium-ion batteries and beyond, *MRS Bull.* 40 (2015) 1067–1078.
- [5] B. Kang, G. Ceder, Battery materials for ultrafast charging and discharging, *Nature* 458 (2009) 190–193.
- [6] K. Xu, Nonaqueous liquid electrolytes for lithium-based rechargeable batteries, *Chem. Rev.* 104 (2004) 4303–4417.
- [7] K. Xu, Electrolytes and Interphases in Li-Ion Batteries and Beyond, *Chem. Rev.* 114 (2014) 11503–11618.
- [8] W. Xu, J. Wang, F. Ding, X. Chen, E. Nasybulin, Y. Zhang, J.-G. Zhang, Lithium metal anodes for rechargeable batteries, *Eng. Environ. Sci.* 7 (2014) 513–537.
- [9] A.M. Haregewoin, A.S. Wotango, B.J. Hwang, Electrolyte additives for lithium ion battery electrodes: progress and perspectives, *Eng. Environ. Sci.* 9 (2016) 1955–1988.
- [10] M. Yoshio, H.Y. Wang, K. Fukuda, Spherical carbon-coated natural graphite as a lithium-ion battery-anode material, *Angew. Chem., Int. Ed.* 42 (2003) 4203–4206.
- [11] T. Ohzuku, Y. Iwakoshi, K. Sawai, Formation of lithium-graphite intercalation compounds in nonaqueous electrolytes and their application as a negative electrode for a lithium ion (Shuttlecock) cell, *J. Electrochem. Soc.* 140 (1993) 2490–2498.
- [12] M. Ko, S. Chae, J. Ma, N. Kim, H.-W. Lee, Y. Cui, J. Cho, Scalable synthesis of silicon-nanolayer-embedded graphite for high-energy lithium-ion batteries, *Nat. Energy* 1 (2016) 16113.
- [13] W.J. Zhang, A review of the electrochemical performance of alloy anodes for lithium-ion batteries, *J. Power Sources* 196 (2011) 13–24.
- [14] N. Liu, Z.D. Lu, J. Zhao, M.T. McDowell, H.W. Lee, W.T. Zhao, Y. Cui, A pomegranate-inspired nanoscale design for large-volume-change lithium battery anodes, *Nat. Nanotechnol.* 9 (2014) 187–192.
- [15] M.N. Obrovac, V.L. Chevrier, Alloy negative electrodes for Li-Ion batteries, *Chem. Rev.* 114 (2014) 11444–11502.
- [16] H.H. Zheng, J. Li, X.Y. Song, G. Liu, V.S. Battaglia, A comprehensive understanding of electrode thickness effects on the electrochemical performances of Li-ion battery cathodes, *Electrochim. Acta* 71 (2012) 258–265.
- [17] M.G. Kim, J. Cho, Air stable Al_2O_3 -coated Li_2NiO_2 cathode additive as a surplus current consumer in a Li-ion cell, *J. Mater. Chem.* 18 (2008) 5880–5887.
- [18] M. Noh, J. Cho, Role of Li_6CoO_4 cathode additive in Li-Ion cells containing low coulombic efficiency anode material, *J. Electrochem. Soc.* 159 (2012) 1329–1334.
- [19] Y. Sun, H.-W. Lee, Z.W. Seh, N. Liu, J. Sun, Y. Li, Y. Cui, High-capacity battery cathode prelithiation to offset initial lithium loss, *Nat. Energy* 1 (2016) 15008.
- [20] Y. Sun, H.W. Lee, G.Y. Zheng, Z.W. Seh, J. Sun, Y.B. Li, Y. Cui, In situ chemical synthesis of lithium fluoride/metal nanocomposite for high capacity prelithiation of cathodes, *Nano Lett.* 16 (2016) 1497–1501.
- [21] A. Abouimrane, Y.J. Cui, Z.H. Chen, I. Belharouak, H.B. Yahia, H.M. Wu, R. Assary, L.A. Curtiss, K. Amine, Enabling high energy density Li-ion batteries through Li_2O activation, *Nano Energy* 27 (2016) 196–201.
- [22] K. Park, B.C. Yu, J.B. Goodenough, Li_3N as a cathode additive for high-energy-density lithium-ion batteries, *Adv. Energy Mater.* 6 (2016) 1502534.
- [23] Y. Sun, Y. Li, J. Sun, Y. Li, A. Pei, Y. Cui, Stabilized Li_3N for efficient battery cathode prelithiation, *Energy Storage Mater.* 6 (2017) 119–124.
- [24] N.A. Liu, L.B. Hu, M.T. McDowell, A. Jackson, Y. Cui, Prelithiated silicon nanowires as an anode for lithium ion batteries, *ACS Nano* 5 (2011) 6487–6493.
- [25] J. Hassoun, K.S. Lee, Y.K. Sun, B. Scrosati, An advanced lithium ion battery based on high performance electrode materials, *J. Am. Chem. Soc.* 133 (2011) 3139–3143.
- [26] H.J. Kim, S. Choi, S.J. Lee, M.W. Seo, J.G. Lee, E. Deniz, Y.J. Lee, E.K. Kim, J.W. Choi, Controlled prelithiation of silicon monoxide for high performance lithium-ion rechargeable full cells, *Nano Lett.* 16 (2016) 282–288.
- [27] Z.H. Wang, Y.B. Fu, Z.C. Zhang, S.W. Yuan, K. Amine, V. Battaglia, G. Liu, Application of stabilized lithium metal powder (SLMP (R)) in graphite anode – a high efficient prelithiation method for lithium-ion batteries, *J. Power Sources* 260 (2014) 57–61.
- [28] M.W. Forney, M.J. Ganter, J.W. Staub, R.D. Ridgley, B.J. Landi, Prelithiation of silicon-carbon nanotube anodes for lithium ion batteries by stabilized lithium metal powder (SLMP), *Nano Lett.* 13 (2013) 4158–4163.
- [29] L. Wang, Y.B. Fu, V.S. Battaglia, G. Liu, SBR-PVDF based binder for the application of SLMP in graphite anodes, *RSC Adv.* 3 (2013) 15022–15027.
- [30] Z. Cao, P. Xu, H. Zhai, S. Du, J. Mandal, M. Dontigny, K. Zaghib, Y. Yang, Ambient-air stable lithiated anode for rechargeable Li-ion batteries with high energy density, *Nano Lett.* 16 (2016) 7235–7240.
- [31] J. Zhao, Z. Lu, N. Liu, H.-W. Lee, M.T. McDowell, Y. Cui, Dry-air-stable lithium silicide-lithium oxide core-shell nanoparticles as high-capacity prelithiation reagents, *Nat. Commun.* 5 (2014) 5088.
- [32] J. Zhao, Z.D. Lu, H.T. Wang, W. Liu, H.W. Lee, K. Yan, D. Zhuo, D.C. Lin, N. Liu, Y. Cui, Artificial solid electrolyte interphase-protected Li_6Si nanoparticles: an efficient and stable prelithiation reagent for lithium-ion batteries, *J. Am. Chem. Soc.* 137 (2015) 8372–8375.
- [33] J. Zhao, H.-W. Lee, J. Sun, K. Yan, Y. Liu, W. Liu, Z. Lu, D. Lin, G. Zhou, Y. Cui, Metallurgically lithiated SiO_x anode with high capacity and ambient air compatibility, *Proc. Natl. Acad. Sci.* 113 (2016) 7408–7413.
- [34] K.H. Seng, M.H. Park, Z.P. Guo, H.K. Liu, J. Cho, Self-assembled germanium/carbon nanostructures as high-power anode material for the lithium-ion battery, *Angew. Chem., Int. Ed.* 51 (2012) 5657–5661.
- [35] Y.H. Xu, Y.J. Zhu, Y.H. Liu, C.S. Wang, Electrochemical performance of porous carbon/tin composite anodes for sodium-ion and lithium-ion batteries, *Adv. Energy Mater.* 3 (2013) 128–133.
- [36] M.T. McDowell, S.W. Lee, W.D. Nix, Y. Cui, 25th anniversary article: understanding the lithiation of silicon and other alloying anodes for lithium-ion batteries, *Adv. Mater.* 25 (2013) 4966–4984.
- [37] L. Wang, Y.J. Chen, J.M. Ma, L.B. Chen, Z. Xu, T.H. Wang, Hierarchical SnO_2 nanospheres: bio-inspired mineralization, vulcanization, oxidation techniques, and the application for NO sensors, *Sci. Rep.* 3 (2013) 3500.
- [38] W.M. Zhang, J.S. Hu, Y.G. Guo, S.F. Zheng, L.S. Zhong, W.G. Song, L.J. Wan, Tin-nanoparticles encapsulated in elastic hollow carbon spheres for high-performance anode material in lithium-ion batteries, *Adv. Mater.* 20 (2008) 1160–1165.